

## Chapter 2

# Experimental Methods

This chapter will introduce the relevant technologies and experimental methods employed for the work of the thesis. It mainly includes the sample preparation techniques: pulsed laser deposition (PLD) and magnetron sputtering; the sample measurement and characterization techniques: (i) the experimental methods used to characterize the macroscopic magnetic properties of the samples, including the superconducting quantum interference device (SQUID), electron spin resonance (ESR), magneto-optical Kerr effect (MOKE) techniques; (ii) the experimental methods used to characterize the macroscopic ferroelectric and piezoelectric properties of the samples, including ferroelectric hysteresis loops and strain curves measurement techniques; (iii) the experimental methods used to characterize the microscopic magnetic and ferroelectric properties, including scanning probe microscopy (SPM), X-ray diffraction (XRD), and transmission electron microscopy (TEM) techniques; and the electric transport measurement techniques used for the investigation of electric field tunable spintronic devices.

## 2.1 Sample Preparation Techniques

### 2.1.1 Pulsed Laser Deposition Method

With the development of laser technology and the relevant applications, a new kind of thin film preparation technology which employs laser as the heat source, i.e., pulsed laser deposition, was first attempted by Smith et al. Later it was developed by Vankatesan et al. in Bell Laboratories of the USA [1] and was widely used in the preparation of high-temperature superconducting, ferroelectric materials, and magnetic oxides.

The principle and basic configuration of the pulsed laser deposition [2, 3] is shown in Fig. 2.1. When a high-energy pulsed laser beam emitted by a laser generator passes through a series of optical system and is finally focused on the target inside a chamber, the temperature of the target surface is instantaneously heated up

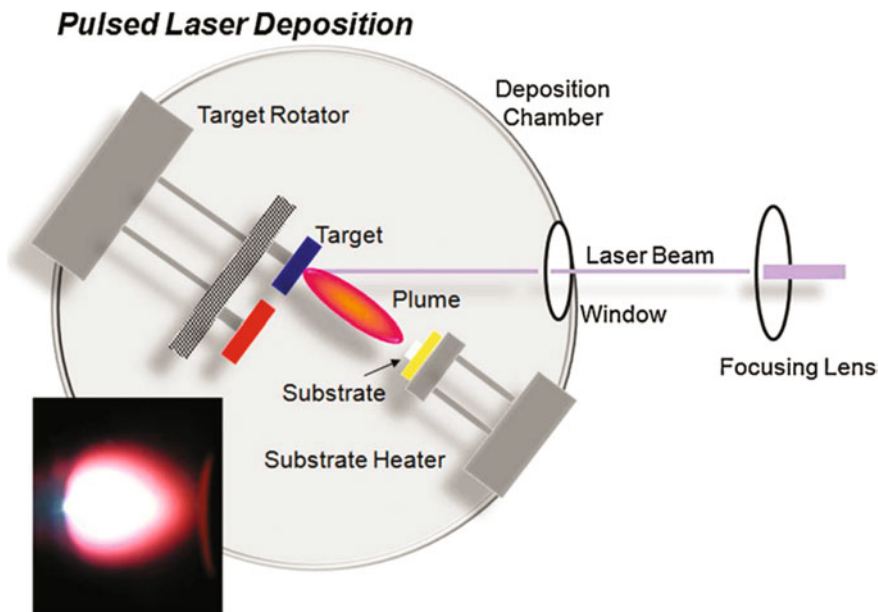


**Fig. 2.1** Schematic diagram of the PLD technology (Reprinted from Ref. [3], Copyright 2010, with permission from Elsevier)

to 2000–3000 K by the high-energy density released from the focused laser beam. Due to the high temperature, the materials inside the target are instantaneously vaporized and ionized, forming complex plasma containing atoms, molecules, ions, and neutral particles. With the continuous absorption of laser energy and further ionization of the materials in the target, the temperature and pressure inside the plasma increase rapidly. As a result, the plasma was ejected perpendicular to the target surface due to the ultra-high-pressure gradient and forms a plume (plasma plume). In the diffusion process of the plasma plume, the interaction between the plasma and the atmosphere inside the chamber will continuously increase the ionization process and the collisions between the components of the plasma, which is finally sprayed onto a substrate placed on a heater. By optimizing the factors such as laser density, pressure of the atmosphere, and heating temperature, epitaxial thin films can be prepared with a right copy of material composition of the targets.

Preparing thin films based on the kinetic and thermodynamic process, the PLD technology has the following characteristics. The advantages are (i) Good component reproduction: Since the majority of the target surface can be ionized into plasma under the heating of the high-energy laser shot, the composition of the film has a high consistency with the target components, which is advantageous for the preparation of the polyhydric compound thin film. (ii) High preparing efficiency and target utilization: Since the plasma plume produced by the laser is always perpendicular to the target surface and sprays directly toward the substrate with a high concentration, PLD has a higher efficiency in thin film deposition and target

utilization than other film preparation methods, which is especially advantageous for preparing films containing toxic elements such as Pb. (iii) It can be operated under higher atmosphere pressure, especially for the film growth which requires an oxygen atmosphere. (iv) It can solve the problem of film preparation of many refractory materials, such as silicides, oxides, carbides, and borides, as the temperature of the target surface can be easily heated as high as 2000–3000 K to vapor any kinds of materials by the highly concentrated laser, which is difficult to achieve in other deposition techniques. In another aspect, PLD technique also has some drawbacks: (i) It is difficult to prepare uniform thin film with a large area, because the plume generated from the target by the irradiation of laser is highly directional with a solid angle  $2\theta_{\max} < 30^\circ$ , which is disadvantageous to prepare thin film with a uniform thickness and a large area. In order to overcome this drawback, a variety of complicated scanning methods are used, such as the substrate scanning, target scanning, and laser scanning. (ii) The film surface prepared by PLD may not be smooth and uniform enough compared with other methods, as the plume generated from the sintered polycrystalline target under the excitation of the high-energy, high-intensity, and high-momentum pulsed laser contains some large neutral particles in addition to the atoms, molecules, ions, etc., which results in the uneven growth of the thin film. In addition to optimizing the deposition conditions, methods of secondary laser ionization as well as placing velocity filter between the target and substrate are employed to prevent the large particles in the plume from arriving at the substrate and solve this problem. It is worth mentioning that the PLD system was equipped with a reflection high-energy electron diffraction (RHEED) for in situ monitoring the film growth process by Kanai et al. in the year 1991 [4], and a new updated PLD system named laser molecular beam epitaxy (laser MBE) was born, which marks a new stage in the development of PLD technology and is sufficient for the preparation of high-quality film by this method.

In the film preparing process via PLD technology, there are mainly three kinds of growth modes depending on factors such as the lattice mismatch between the film and substrate, surface energy of the film, and interface energy. They are island growth, layered growth, and mixed growth, as shown in Fig. 2.2.

(i) Island growth (Volmer–Weber mode, island growth, 3D): Due to the poor wettability between the film and the substrate, the film surface tends to form a smaller contact with the substrate, resulting in an island-like distribution of atom nucleation at the interface and three-dimensional growth of the nucleus. With the continuous growth of the atom islands during the deposition, islands are connected with each other and finally form the thin film. (ii) Layered growth (Frank-van der Merwe mode, layer-by-layer growth, 2D): Due to the good wettability between the film and the substrate, the film surface tends to form a larger contact with the substrate, resulting in a two-dimensional extension of atom nucleation at the interface and layer-by-layer growth of the thin film. (iii) Mixed growth (Stranski–Krastanov mode, layer plus island growth, 2D–3D): Despite the good wettability between the film and the substrate, the lattice parameters of the film and the substrate do not match with each other. As a result, the film first grows layer-by-layer to

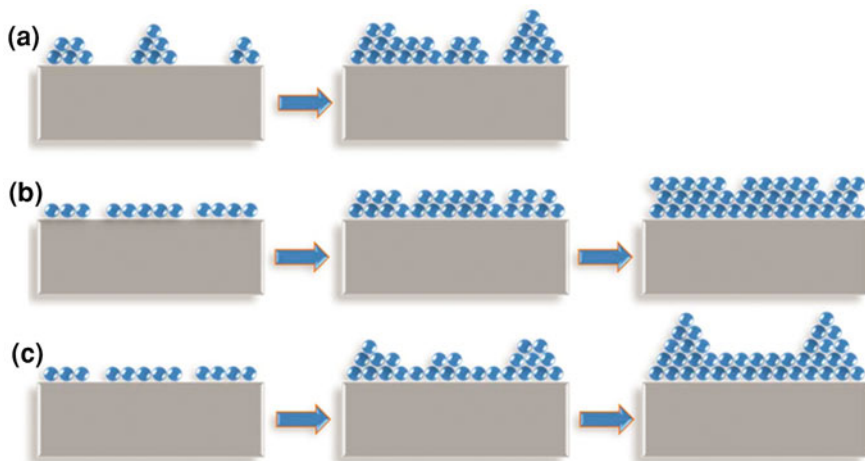


**Fig. 2.2** Three kinds of film growth modes in PLD technology: **a** island growth, **b** layer-by-layer growth, **c** mixed growth (Reprinted from Ref. [3], Copyright 2010, with permission from Elsevier)

reduce the interface energy and then it changes to island growth to reduce the strain energy.

Since the PLD technique can achieve the epitaxial growth of crystalline thin films without special limitation and requirements of the materials, it is easy to use this method for epitaxially growing different materials onto different substrates, forming different heterostructures or superlattice. Due to the lattice parameter mismatches between the films and substrates made from different materials, there are different epitaxial modes in film growth, including nearly perfectly lattice matched film growth, strained film growth, and relaxed heteroepitaxial film growth, as shown in Fig. 2.3, which can ultimately achieve the exact control of the film or interface resulting in interesting physical phenomena and issues [3].

### 2.1.2 Magnetron Sputtering Method

Magnetron sputtering is a kind of thin film preparing technology, in which high-energy particles or ions are employed to bombard the target for providing materials source for the thin film growth under the combined effects of the electric and magnetic fields, as shown in Fig. 2.4. The atoms and molecules of the target materials are sputtered out and deposited onto the substrate, as a result, a thin film with the component of the target materials can be prepared [5].

The working principle of the magnetron sputtering is described as follows. The target for sputtering is used as the cathode, behind which there is a piece of strong magnet (about 1,000 Gauss). The substrate to grow the thin film is used as the anode and placed on the substrate stage opposite the target. Before sputtering, the

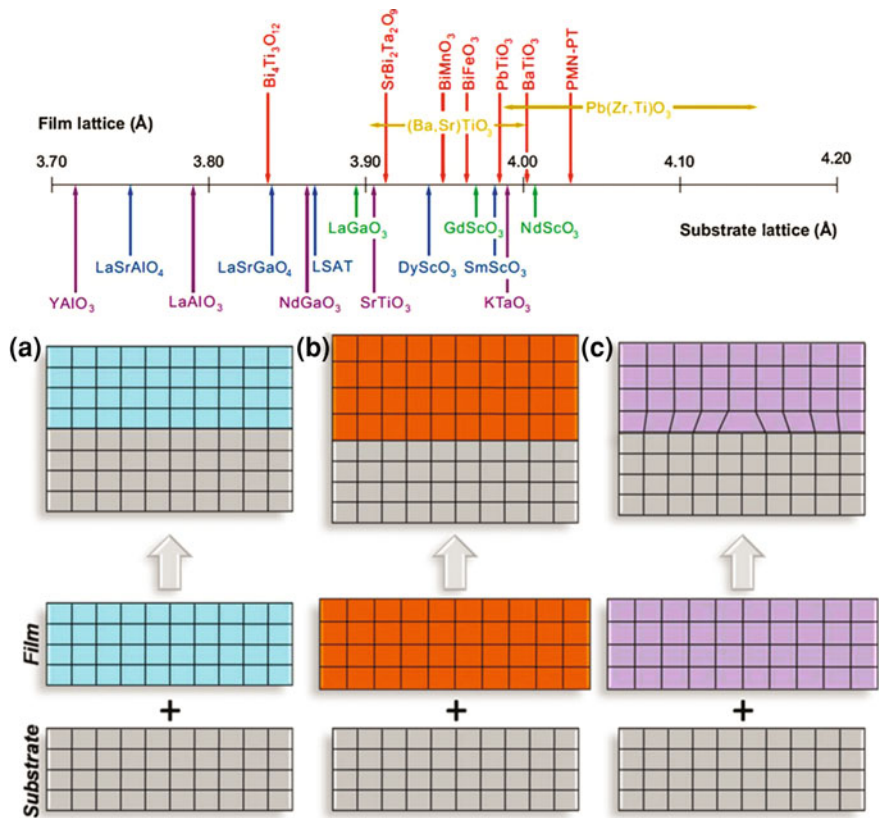


**Fig. 2.3** Lattice parameters of different materials and different epitaxial modes: **a** matched growth, **b** strained growth, **c** relaxed heteroepitaxial growth (Reprinted from Ref. [3], Copyright 2010, with permission from Elsevier)

**Fig. 2.4** Configuration of the magnetron sputtering device

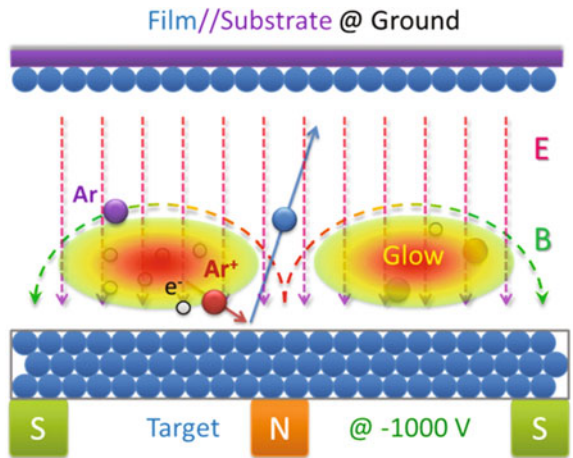
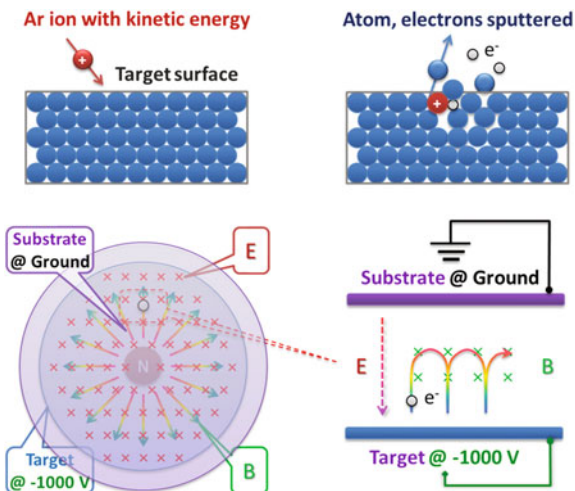


**Fig. 2.5** Cycloid movement of the secondary electrons during sputtering



chamber should be pumped into vacuum and filled with a certain amount of inert gas (Ar) with the pressure about 0.1 Pa, which can be served as the carrier during discharge. When the high voltage is turned on, the electrons are accelerated by the electric field and rush toward the anode. During the running process from the cathode to the anode, the electron may collide with the argon atom, ionizing it and producing an  $\text{Ar}^+$  ion and a new electron (secondary electron). The negatively charged electron continuously flies toward the anode, and the positively charged  $\text{Ar}^+$  ion accelerates under the strong electric field, moves toward the cathode, and finally hits into the target surface with a high energy, engaging the sputtering. In the sputtering process, the neutral atoms or molecules of the target are bombarded exited from the target surface by the  $\text{Ar}^+$  ions, sputtering onto the substrate and forming a thin film. The secondary electrons will be subject to the combined action of electric field and circular magnetic field after leaving the target surface, repeating a specific performance as follows. The secondary electron first enters the dark region near the cathode, in which it is accelerated by the electric field ( $E$ ) and begins to fly toward the glow region. Once in the glow region, the electron is exposed to the magnetic field ( $B$ ) and begins to rotate perpendicular to the magnetic field driven by the Lorentz force. After flying a half circle in the glow region, the electron returns to the dark region again near the cathode. Inside this dark region, the velocity of the electron is slowed down and reversed under the action of electric field. As a result, this electron speeds up again under the electric field and flies toward the glow region to start a new cycle. Thus, the electrons perform a circular cycloid motion repeatedly and drift around the target surface, as shown in Fig. 2.5. This ingenious design of magnetron sputtering extends the movement path of the electrons and bounds the electrons inside the plasma near the target surface, by means of which the probability of collision between the electrons and the inert gas and the efficiency of the energy utilizing of the electrons have been largely increased, ultimately making the sputtering more effective.

Compared with PLD, the magnetron sputtering method has the following advantages. (i) It can be used to grow thin films with a large area, good uniformity, and high flatness. (ii) Since the conditions of magnetron sputtering are relatively fixed, the deposition rate is pretty stable. By precisely controlling the sputtering time, the accurate thickness of the film can be easily controlled with good repeatability. (iii) Since the energy of electron or atom arriving at the substrates is relatively low, there is no obvious thermal effect generated on the substrate, which is important for the growth of some heat-sensitive materials. If needed, a cooling system can be integrated inside the substrate stage to keep the substrate at a certain low temperature and meet some special requirements. The disadvantages of the magnetron sputtering are mainly as follows. (i) In the preparation of multicomponent film, the sputtering efficiencies of different components in the target are different. As a result, the components of thin film prepared are not consistent with the components of the target, which is known as component segregation. (ii) Since the distribution of the magnetic field is limited inside a small circular space around the target, only a small circular region of the target is corroded by the ions during sputtering, forming a deep annular groove in the target. This nonuniform consumption of the target causes a serious waste of the target, with the utilization efficiency less than 50 %.

Overall, magnetron sputtering technology is a kind of effective film preparation method. With the continuous development of the relevant technologies, magnetron sputtering has been widely and successfully used in many areas, especially in the preparation of microelectronic devices, optical thin films, and the surface treatment of different materials, with a great significance [6].

## **2.2 Measurement, Characterization, and Analysis Techniques for Multiferroic Properties**

### ***2.2.1 Measurement and Characterization of Macroscopic Magnetic Properties***

Technologies used for characterization of the magnetic samples are various, while only a few of the magnetism measurement technologies related to the thesis work are introduced here. They are superconducting quantum interference devices (SQUID) used for measuring magnetization and magnetic hysteresis loop, electron spin resonance (ESR), and magneto-optical Kerr effect (MOKE) used for measuring the magnetic anisotropy.

*Superconducting quantum interference device* (SQUID) is an apparatus used for measuring weak magnetic signals or magnetic moments via the quantum interference effect of the superconductor, due to its sensitivity to the magnetic flux. The core assembly of the SQUID is called Josephson tunnel junction, which consists of

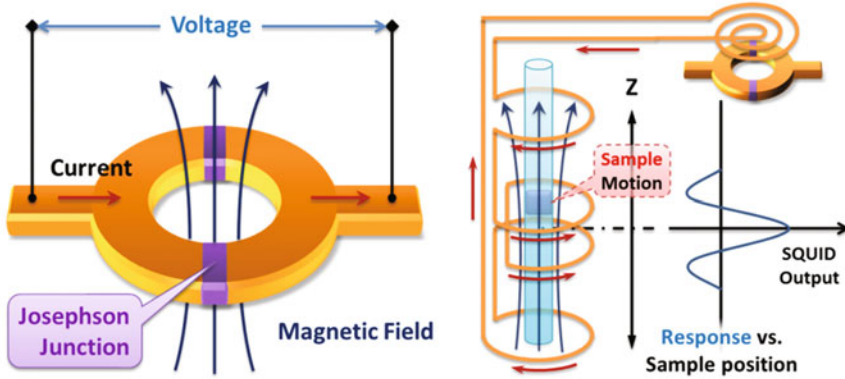
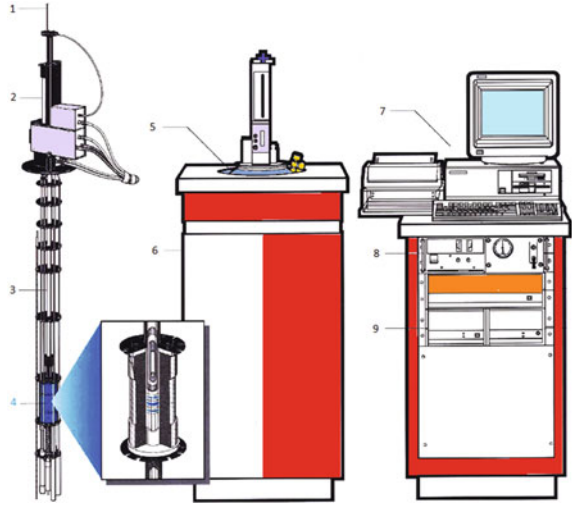


**Fig. 2.6** Configuration of Josephson junction (*left*) and the basic principle of SQUID (*right*)

two pieces of superconductors separated by a thin barrier layer. When the Josephson tunnel junction is connected to a superconducting circuit, a kind of macroscopic quantum interference phenomenon will present. That is, the voltage across the Josephson tunnel junction exhibits a periodic function with the change of magnetic flux inside the circuit. When a magnetic sample is moving in the superconducting coil, the change in the external magnetic flux will induce a change in superconducting current in the circuit. Due to the coupling attenuation in the SQUID, the changed current will change the magnetic flux in the Josephson tunnel junction and finally change the voltage of the device. SQUID is essentially a magnetic flux-voltage converter which can output voltage with amplitude proportional to the detected magnetic signal, as shown in Fig. 2.6. The minimum magnetic flux which can cause quantum interference phase change in the Josephson tunnel junction is a single flux quantum ( $\Phi_0 = 2.07 \times 10^{-15}$  Wb), thereby the SQUID has an ultra-high-sensitivity in detecting the magnetization [7, 8].

In addition to the function of accurate magnetization measurement, the SQUID is also an integrated magnetic property measurement system (MPMS) controlled by a computer with the ability of measuring all kinds of magnetic properties, such as saturated magnetization, coercivity, Curie temperature, and susceptibility, under variable temperatures and magnetic fields, as shown in Fig. 2.7. The MPMS employs a heater and liquid helium cooling system to control the temperature and utilizes the superconducting coil to generate strong and precision magnetic fields. Combined with different electrometers, the measurement of the electrical properties of the sample varying with temperature and magnetic field, such as the spin-dependent transport, can be achieved. The SQUID used in the work related to this thesis is a Quantum Design MPMS-XL, with the abilities of accurately controlling the temperature in the range of 1.9–800 K with a maximum rate up to 10 K per minute, accurately controlling the magnetic field in the range of  $-7.0$  to  $7.0$  T with the precision of  $0.2$  Oe, and accurately measuring the magnetic moments in the range of  $-2.0$  to  $2.0$  emu with the resolution of  $1 \times 10^{-8}$  emu.

**Fig. 2.7** Configuration and basic hardware parts of the MPMS: 1 sample rod, 2 sample transport, 3 sample chamber, 4 superconducting coils, 5 Dewar, 6 isolation cabinet, 7 computer, 8 controller units, 9 power units (Reprinted with permission from Ref. [8], Copyright Quantum Design 1994)



Despite the varied functions in measuring the magnetic properties, the existing MPMS cannot take the magnetic measurements under in situ electric fields, which is important for investigating ME coupling effect of the multiferroics in this thesis. After the pioneer work of a previous member in our group [9], we have developed MPMS and achieved the technique of measuring the magnetic properties under in situ electric field, which is significant for the investigation of multiferroic materials.

*Magnetic resonance* is a kind of phenomenon where materials with nonzero magnetic moments of atoms or nuclei exhibit obvious resonance absorption of the electromagnetic radiation under a static magnetic field, including nuclear magnetic resonance (NMR), paramagnetic resonance (PMR), optical magnetic resonance (OMR), and ferromagnetic resonance (FMR). If the magnetic resonance is caused by the magnetic moment of the electron spin in the material, it is called electron spin resonance (ESR) or electron paramagnetic resonance (EPR). Materials with unpaired electrons can be studied by the ESR method, such as atoms and molecules with an odd number of electrons, ions with unfilled inner electron shells, and radicals induced by radiation damage. The ESR spectra of the sample can give the information or states of the molecules, atoms, and ions related to the spin of electrons, and therefore, the ESR method has become an important experimental technique in modern physics, with wide applications in physics, chemistry, materials science, biology, medicine, and many other fields [10].

The basic principle of the ESR measurement is as follows. As we know, the spin orientations of an isolated electron have only two possible directions, which produce two possible spin-related magnetic moments  $\pm\mu_B$  ( $\mu_B$  is called Bohr magneton). When the electron is in an external magnetic field, the magnetic potential energy provided by the magnetic field will split the spin of the electron into two states (Zeeman effect), with the energy gap proportional to the magnetic

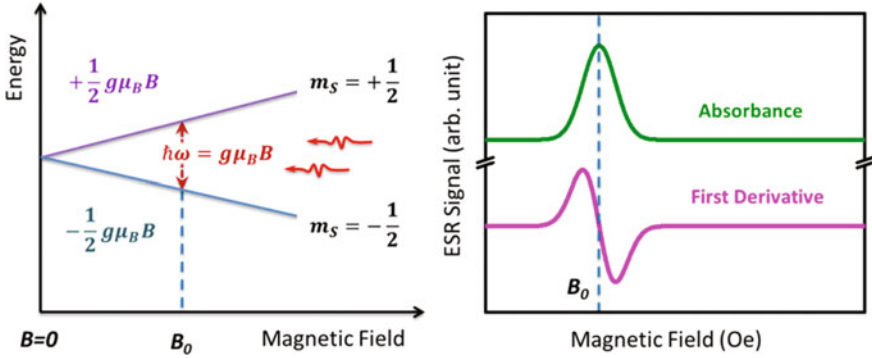


**Fig. 2.8** Principle of ESR (*left*) and derivation of the resonance field (*right*)

field  $\Delta E = g\mu_B B$  ( $g$  is called the electron spin  $g$ -factor). If an electromagnetic wave with an appropriate frequency  $\hbar\omega = \Delta E$  is applied along the vertical direction of the magnetic field, a transition from the low-energy spin state to the high-energy spin state can be induced, accompanied with a strong absorption of the incident electromagnetic wave and producing the ESR signal. By measuring the resonance frequency  $\omega$  and the corresponding external magnetic field  $B$ , the electron spin  $g$ -factor can be calculated and the atomic structure as well as other information related to the electron spin can be deduced. The resonance condition  $\hbar\omega = g\mu_B B$  can be achieved by either scanning the magnetic field  $B$  under fixed frequency  $\omega_0$  or scanning the frequency  $\omega$  under fixed magnetic field  $B_0$ . We employ the method of scanning magnetic field under fixed frequency to investigate the magnetic anisotropy in this thesis, from which the resonant magnetic field can be obtained by differentiating the ESR signal, as shown in Fig. 2.8.

*Magneto-Optical Kerr Effect* (MOKE) is one of the magneto-optical effects which occur in the interaction between light and magnetic materials. When a beam of linearly polarized light is incident to a magnetic thin film, part of the light will transmit through the magnetic material and part of the light will be reflected from the magnetized surface. The polarization directions as well as the intensities of both the transmitted light and reflected light will be changed, which are known as magneto-optical effects and can be divided into two kinds. The one that describes changes in light in the transmitted case is called Faraday effect, and the other that describes changes in light in the reflected case is called Kerr effect [11]. Thereby, the angles between the incident light and transmitted/reflected lights are called magneto-optical Faraday/Kerr rotation angles ( $\theta_F/\theta_K$ ), respectively, as shown in Fig. 2.9.

There are three kinds of configurations that are mostly used in the investigation of magnetic samples by MOKE, including (i) polar Kerr effect, in which the magnetization vector is parallel to the plane of incidence and perpendicular to the sample surface (i.e., reflection surface); (ii) longitudinal Kerr effect, in which the magnetization vector is parallel to both the plane of incidence and the sample surface;

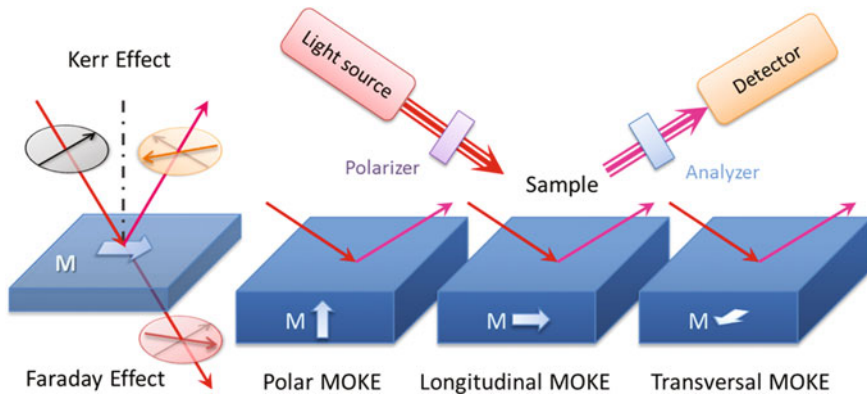


**Fig. 2.9** Classification of the magneto-optical effects and configurations of the Kerr effect

(iii) transversal Kerr effect, in which the magnetization is perpendicular to the plane of incidence and parallel to the sample surface, as shown in Fig. 2.9. Since the results of the MOKE measurement mainly reveal the information about magnetization at the sample surface, the MOKE is also called surface magneto-optical Kerr effect (SMOKE). Moreover, the amplitude and direction of the Kerr rotation angle  $\theta_K$  are related to the magnetization states of the sample near the surface. As a result, the local and surface magnetic hysteresis loop ( $M-H$ ) can also be obtained by the SMOKE method.

Considering the advantages and characteristics of the three kinds of magnetic measurement methods discussed above, we employ SQUID for the main magnetic measurements, such as magnetic hysteresis loops ( $M-H$ ) and in situ electrical control of magnetization, ESR to investigate the bulk magnetic anisotropy, and MOKE to detect the local and surface magnetic properties as well as the magnetic anisotropy evolution of the sample under in situ electric fields, respectively.

### 2.2.2 Characterization of Macroscopic Ferroelectric and Piezoelectric Properties

The most important feature indicating the ferroelectricity of material is the existence of spontaneous polarization and ferroelectric hysteresis loop, in which the polarization  $P$  can be switched hysteretically by an external electric field  $E$ . As a result, the ferroelectric hysteresis loop is also called  $P-E$  loop. From the  $P-E$  loop, the important parameters of the ferroelectric material, such as the spontaneous polarization  $P_S$  and the coercive electric field  $E_C$ , can be learned. Thereby, the  $P-E$  loop measurement of the ferroelectric materials is an important method to characterize the ferroelectric properties.

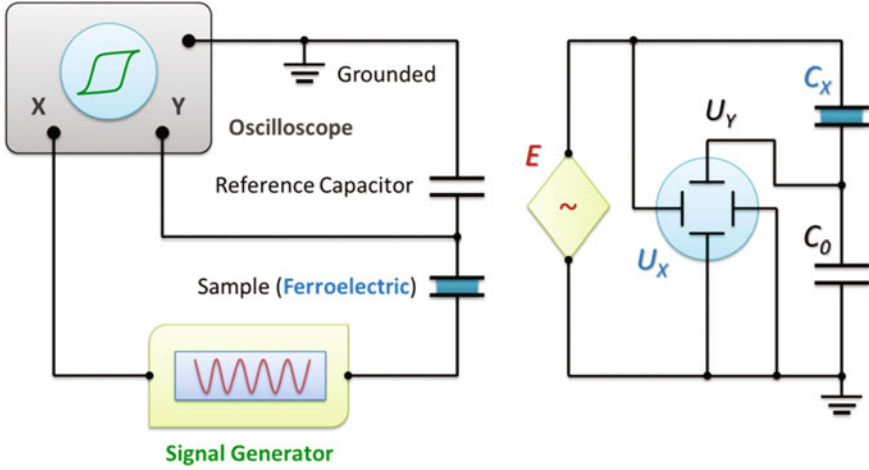


**Fig. 2.10** Configuration of the Sawyer-Tower circuit (*left*) and the equivalent circuit (*right*)

A conventional and most often quoted method for the  $P$ - $E$  loop measurement is called Sawyer-Tower circuit [12], which consists of an oscilloscope, a signal generator  $E$ , a reference capacitor  $C_0$ , and another capacitor  $C_x$  with the ferroelectric sample to be measured, as shown in Fig. 2.10. The basic principle and detailed working process are as follows. The signal generator generates an alternating electric signal in the circuit, which changes the current and charge in the electronic devices. Since the reference capacitor  $C_0$  and the sample capacitor  $C_x$  are series wound, they are loaded with the same amount of charge  $Q$ . For the situation of the reference capacitor  $C_0$ , there is equation  $Q = C_0 \times U_y$ , in which  $U_y$  is the voltage of  $C_0$ . Therefore, the charge  $Q$  of the sample capacitor  $C_x$  can be deduced from the reference capacitance  $C_0$  and the voltage  $U_y$  across it. As for the sample capacitor  $C_x$ , the polarization  $P$  of the ferroelectric sample is proportional to the charge  $Q$  of it according to the equation  $Q = P \times A$ , where  $A$  is the area of the electrode on the sample. Overall, the polarization  $P$  of the sample is proportional to the voltage  $U_y$  of the reference capacitor, so the electric signal  $U_y$  can wholly represent the ferroelectric polarization  $P$ . In another aspect, the voltages across the reference capacitor and sample capacitor can be expressed by equations  $U_x = Q/C_x$  and  $U_y = Q/C_0$ . In the design of the Sawyer-Tower circuit, the value of the reference capacitance  $C_0$  is larger than that of the sample capacitance  $C_x$ . Therefore, the voltage of the sample capacitance is larger than that of reference capacitance ( $U_x \gg U_y$ ), and  $U_x$  is approximately equal to the voltage of the signal generator  $E$ . Inputting  $U_x$  as the  $x$ -channel of the oscilloscope and  $U_y$  as the  $y$ -channel which represent the driving electric field  $E$  and polarization  $P$  of the sample, respectively, the ferroelectric hysteresis loop can be directly displayed on the oscilloscope.

In the Sawyer-Tower circuit, the reference capacitor  $C_0$  will induce a back voltage to the sample, and a parasitic capacitance  $C_p$  is inevitable during the charge and discharge process, which will affect the accuracy of the ferroelectric hysteresis

loop measurement. To overcome these defects, an integrated circuit with the virtual ground technique is employed for the Premier II-type ferroelectric hysteresis loop measurement system designed by Radiant Company. Using this measurement system, the ferroelectric samples can be effectively and accurately measured with a frequency range of 0.03–100 kHz, charge range of 0.80 fC–5.26 mC, and voltage range from –10 to 10 kV. On the other hand, the widespread problems in the ferroelectric thin film, such as the parasitic conductance (i.e., leakage), parasitic capacitance, and parasitic diode, can be possibly avoided by using the positive-up negative-down (PUND) method [13] or the double-wave method (DWM) [14] in the Radiant Premier II system, with the core idea that the remanent polarization  $P_r$  can be obtained by subtracting the electric signal without polarization switching from the electric signal with polarization switching. Since the most used ferroelectric samples in this thesis work are high-quality PMN-PT single crystals with high polarization and low leakage, the above problems do not exist in the measurement, and therefore, the PUND and DWM methods are not amplified here.

Generally speaking, the ferroelectric material is also piezoelectric, and the piezostain of the sample exhibits a *butterfly* behavior under bipolar electric field due to the polarization switching in the ferroelectrics. Under small electric field, the magnitude of the strain of the ferroelectric material is generally less than 0.1 %, and therefore, precision displacement measurement devices, such as laser interferometer and strain gauge, are employed for the piezostain measurement. Since the strain gauge measurement has advantages such as small size, flexible, and easy to be integrated, it has been successfully used to characterize the strain properties of the ferroelectric materials [15–18]. The basic principle of the strain gauge measurement comes from the law that the resistance of a sample varies with its geometrical dimensions. When the strain gauge and sample (ferroelectric or piezoelectric) are firmly bonded, the strain of the sample induced by the external electric field via converse piezoelectric effect will be transmitted to the strain gauge and changes the geometrical dimensions of the resistance wire, thereby changing the total resistance of the strain gauge. As a result, the strain of the sample can be deduced by measuring the resistance of the strain gauge. Since the strain of the sample is very small, the resistance change of the strain gauge is also small. To detect this slight change in resistance, the quarter-bridge (Wheatstone bridge) is employed to realize the precise strain measurement, as shown in Fig. 2.11. Thanks to the flexibility of the strain gauge-based measurement method, we can easily obtain the strain in any direction of the ferroelectric sample by aligning the sensitive direction of the strain gauge with the interested direction of the sample while bonding. Moreover, by combining the strain gauge with a temperature controlling equipment such as SQUID in an automatic controlling program, we have successfully developed an integrated system with the function of measuring strain as well as other properties of the ferroelectric sample under low temperature, which has expanded the scope of strain investigation in materials. Since the work related to strain measurement in this thesis is mainly at room temperature, the low-temperature strain measurement system is not necessary to be introduced here.

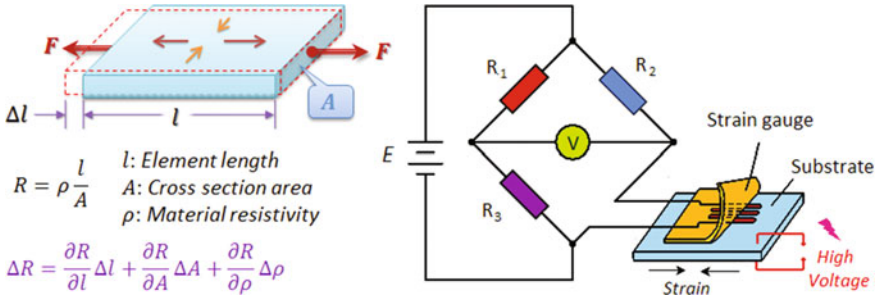


**Fig. 2.11** Basic principle of the strain gauge (left) and configuration of the strain measurement of piezoelectric/ferroelectric samples (right)

### 2.2.3 Characterization of Microscopic Ferromagnetic and Ferroelectric Properties

The microscopic characterization techniques for the multiferroic samples in this thesis are mainly based on the scanning probe microscopy (SPM), which is a new kind of microscopic characterization technology developed from the scanning tunneling microscopy (STM) and involves a variety of new functional microscopies, such as atomic force microscopy (AFM), lateral force microscopy (LFM), magnetic force microscopy (MFM), and piezoresponse force microscopy (PFM). The common feature of these techniques is that they employ a sharp tip to scan the sample surface and probe the local information with contact or non-contact modes, for which they are collectively called SPM [19, 20]. Using different kinds of tips which have different kinds of interactions with the sample surface, different kinds of physical properties of the sample can be probed with the different operating modes in SPM, described as follows.

*The basic principle and work process of AFM* are described as follows. Just as a blind man using a stick to explore the obstacles on the road ahead of him, the AFM technique employs a sharp tip to probe the sample within a very short distance to the surface and scans the tip in two dimensions for imaging. The positions of the tip which contain the height information about the sample surface can be amplified by an optical lever method and detected by the laser beam deflection in a four-quadrant detector, as shown in Fig. 2.12. However, in the real imaging process, the tip maintains a fixed contacting force or tapping amplitude with the sample surface, controlled by a feedback system. Therefore, the height information about the undulating sample surface can be reflected in the feedback system, which finally gives the topography. Since the dominant interactions between the tip and the sample surface are van der Waals forces between molecules and atoms, this kind of microscopic characterization technique is called atomic force microscopy.

*The magnetic force microscopy (MFM)* is a functionalized variant of atomic force microscopy, in which a sharp magnetized tip is employed in the two-dimensional scanning to detect the magnetic signals of the magnetic samples and

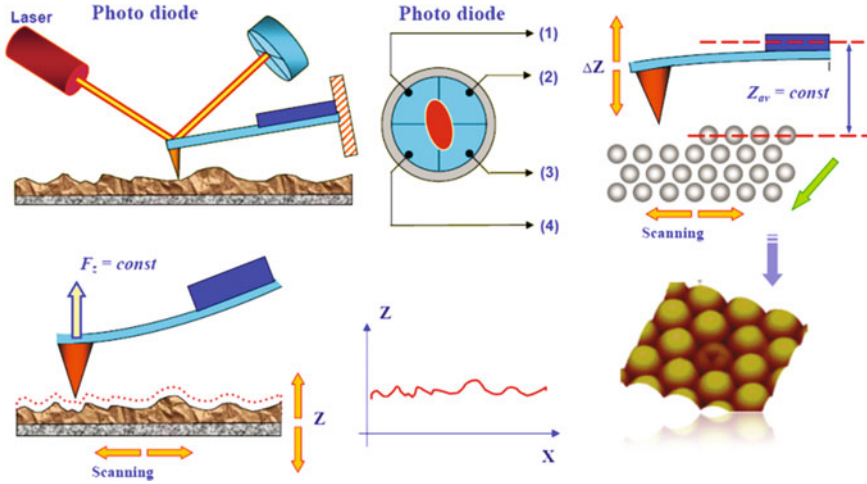


**Fig. 2.12** Basic principle and configuration of AFM (Reprinted with permission from Ref. [20], Copyright 2004 NT-MDT, All right reserved)

reconstruct the magnetic structure of the sample surface [21]. The scanning operation in MFM is relatively complicated with a lift mode, in which each line of the sample surface must be scanned twice. First, the tip carries on the scanning closely to the sample surface ( $<10$  nm), in which not only the magnetic forces are sensed, but also the van der Waals forces. Then, the tip is lifted further away from the sample surface (usually 10–200 nm) and scans the sample along the topographic profile obtained from the first scanning. On this second pass, since the short-range van der Waals force between the tip and the sample atoms does not exist, only the magnetic forces related to the gradient of the leakage magnetic field near the sample surface are detected and the effects of the undulating sample surface can be ruled out by the profile-consulted scanning. As a result, the magnetic signal is extracted and the magnetic domains can be reconstructed together with the topography, as shown in Fig. 2.13. Limited by the working principle, the MFM can only observe the magnetic domain structure perpendicular to the sample surface. However, compared with the optical method used for the magnetic domain observation, the MFM has higher resolution with detailed magnetic information and is significant for the investigation of micromagnetics.

The *piezoresponse force microscopy* (PFM) is another functionalized variant of atomic force microscopy, which utilizes the converse piezoelectric effect to investigate the ferroelectric domain structure or piezoelectric coefficients of ferroelectric samples. The working principle of PFM is described as follows. When a small alternative electric field is applied onto the sample via a conductive tip, different kinds of surface deformation can be induced by the AC voltage depending on the piezoresponse of different ferroelectric domains. For example, ferroelectric domain with polarization downward will always exhibit in-phase piezoelectric resonance, in which the ferroelectric domain stretches under positive

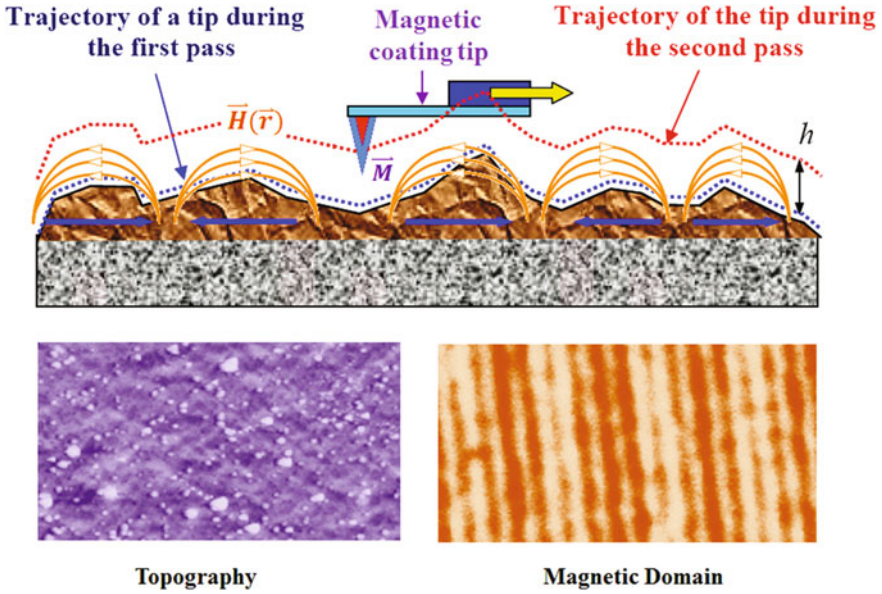


**Fig. 2.13** Basic principle and operation process of MFM (Reprinted with permission from Ref. [20], Copyright 2004 NT-MDT, All right reserved)

electric field and contracts under negative electric field. As for the situation with polarization upward, the piezoresponse of the ferroelectric domain is opposite to the AC driving electric field, which is called out-of-phase piezoelectric resonance. Using the lock-in amplifier, the amplitude and phase information can be deduced from the piezoresponse signal, which reflect the piezoelectric coefficients (such as  $d_{33}$  and  $d_{15}$ ) and the polarization orientations of the ferroelectric domains, as shown in Fig. 2.14. As a result, the ferroelectric domain structure can be reconstructed in terms of amplitude and phase images via the two-dimensional scanning of the sample surface. By PFM, various ferroelectric samples have been successfully characterized with a better understanding of the ferroelectricity in the microscale [22, 23].

In the PFM measurement process, the tip and sample surface keep in contact with each other (contact mode) to detect the piezoresponse of the ferroelectric domains. If the ferroelectric sample under measurement is single crystal with a rhombohedral structure such as  $\text{BiFeO}_3$  [24], the spontaneous polarizations of the sample, which have eight possible directions lying along the diagonal of the pseudo-cubic unit cell, have not only out-of-plane components but also in-plane ones. As a result, the tip on top of the ferroelectric domain can not only feel the piezoelectric component with direction perpendicular to the sample surface, but also feel the piezoresponse along the in-plane direction. The out-of-plane piezoresponse will move the tip up and down under AC driving signal, while the in-plane one will twist the tip left and right. Both the in-plane and out-of-plane tip

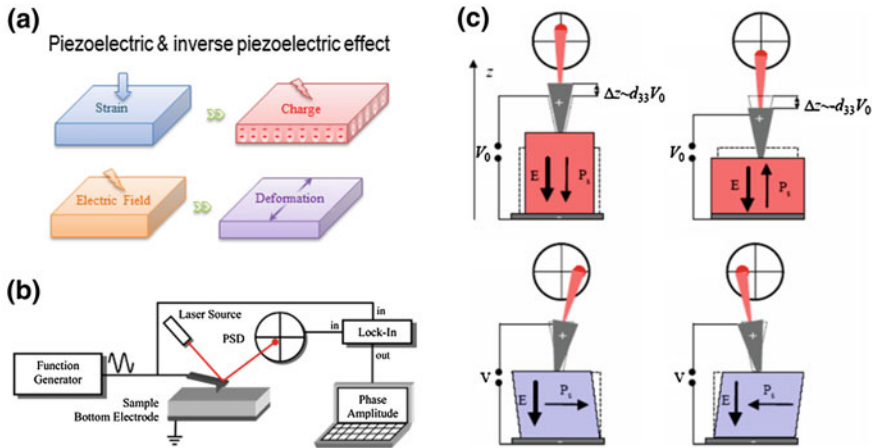


**Fig. 2.14** The **a** piezoelectric effect, **b** configuration and **c** the basic principle of PFM (Reproduced from Ref. [22] by permission of John Wiley & Sons Ltd.)

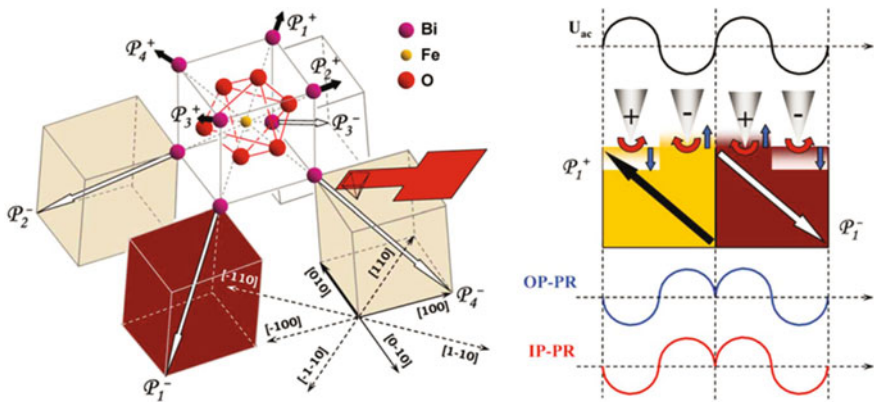


**Fig. 2.15** Piezoresponse of different polarization vectors to the PFM tip (Reprinted from Ref. [24] by permission of Taylor & Francis Ltd.)

movements can be sensed and quantified by the quadrant photodetector, which change the lateral and vertical deflections, respectively. According to the in-plane and out-of-plane piezoresponse obtained by PFM, the domain structure as well as the polarization orientation of the sample can be reconstructed, as shown in Fig. 2.15.

Notably, since the in-plane piezoresponse component with direction parallel to the tip cantilever cannot be detected, the in-plane ferroelectric domain image will exhibit different results depending on the orientation of the tip cantilever. Especially in some directions, the contrast of in-plane phase image will exhibit triple

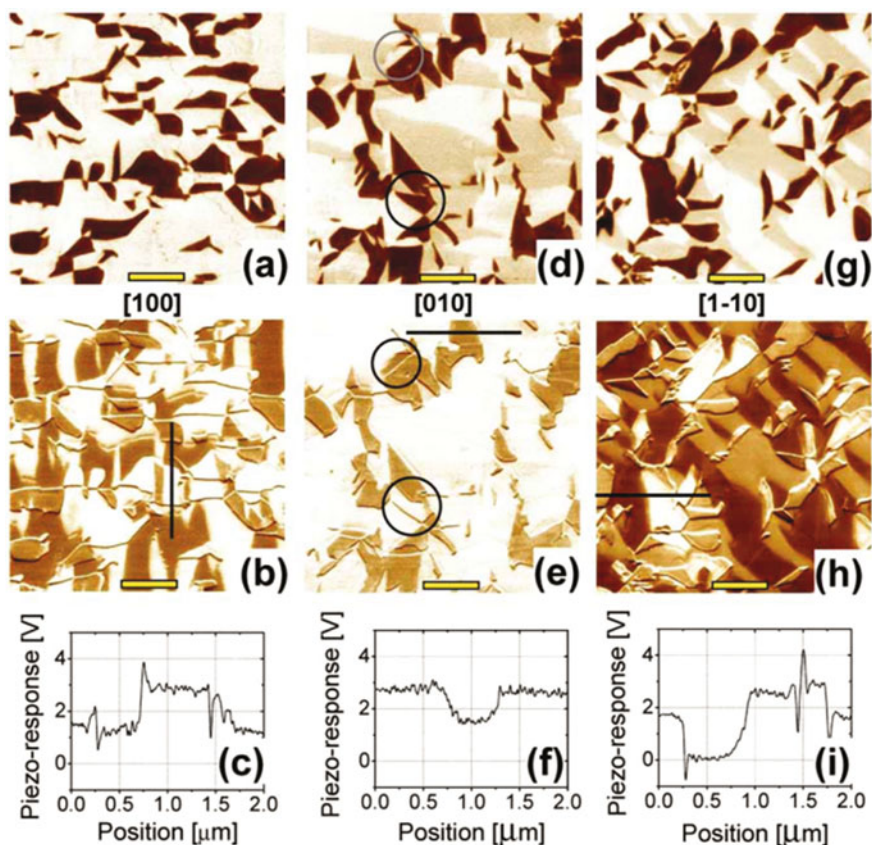


**Fig. 2.16** Out-of-plane (a, d, g) and in-plane (b, e, h) PFM phase images as well as in-plane piezoresponse signals (c, f, i) with tip cantilever along different directions (Reprinted from Ref. [24] by permission of Taylor & Francis Ltd.)

colors, representing polarization pointing left, right, and along the cantilever direction. However, the out-of-plane ferroelectric domain image does not exhibit much difference with the variation in cantilever direction, with a typical two-color contrast in the phase image, as shown in Fig. 2.16.

Moreover, it is also possible to switch the polarizations of the ferroelectric domains by the DC bias voltage applied on the sample through the tip and perform the in situ observation via PFM, as shown in Fig. 2.17, which is helpful to thoroughly investigate the different domain switching categories and further understand the dynamic process of domain switching in ferroelectric materials.

The SPM system used in the work related to this thesis is MultiMode-8 microscope equipped with NanoScope V controller produced by the Veeco Instruments Inc. This SPM system has a variety of functions such as the AFM, MFM, and PFM as described above, by which the surface topography, magnetic

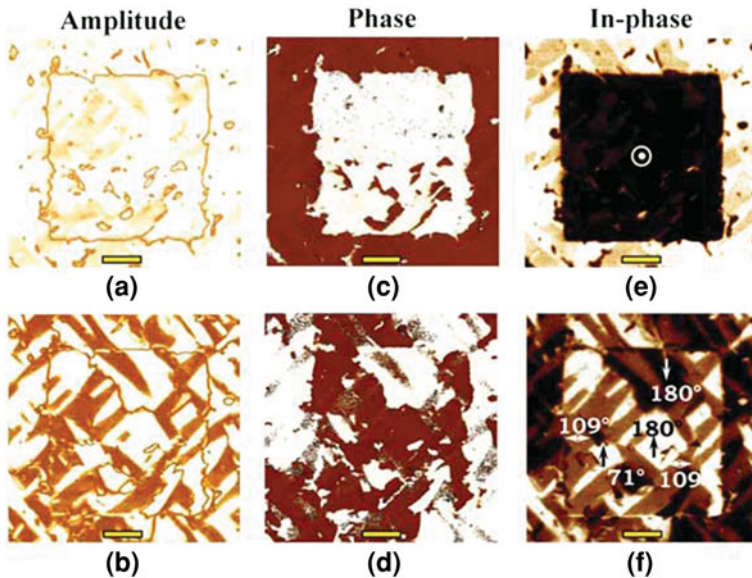


**Fig. 2.17** Domain switching investigation by PFM: **a, b** the amplitude images **c, d** out-of-plane phase images **e, f** in-plane phase images (Reprinted from Ref. [24] by permission of Taylor & Francis Ltd.)

domain, and ferroelectric domain of the sample can be measured. Moreover, photoemission electron microscopy (PEEM) has also been attempted in part of the work to visualize the in-plane magnetic domain [25]. Since the work is mainly completed by collaborators, the PEEM method is not enlarged here.

#### **2.2.4 X-ray Diffraction Techniques and Crystal Structure Analysis**

X-ray diffraction (XRD) is a kind of diffraction phenomenon that originates from the interaction between the X-ray and atoms inside materials. If the material has a crystal structure which consists of atoms with periodic arrangement, regular diffraction patterns will be generated. By analyzing the diffraction patterns, the structure and lattice parameters of the crystal can be deduced. Therefore, XRD has been a powerful and commonly used characterization method in determining the crystal structure, crystallographic plane orientation, texture, and grain size of materials [26].

The basic principle of XRD is described as follows. A beam of collimated X-ray is incident to a crystal surface with lattice parameter  $d$  at an angle  $\theta$ . If the

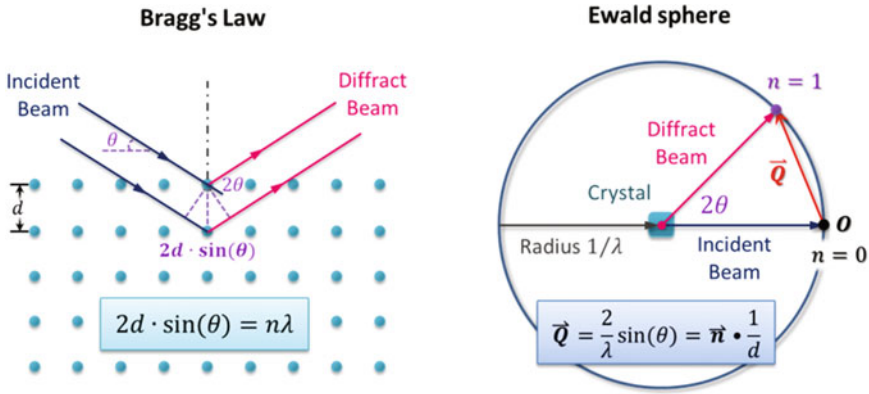


**Fig. 2.18** Bragg's law (*left*) and the Ewald sphere (*right*)

incident light and diffraction light meet certain condition, the diffraction light will be enhanced due to superposition, which generates the regular diffraction spot. The diffraction condition required for the superposition can be simply described by Bragg's law:  $2d_{hkl} \sin(\theta) = n\lambda$ , where  $d_{hkl}$  is the interplanar distance between crystal faces,  $\theta$  is the angle between the incident light and the sample surface,  $n$  is the diffraction order, and  $\lambda$  is the wavelength of the X-ray. The Bragg's law describes the requisite condition for X-ray diffraction in real space. As for the reciprocal space, Bragg's law can be easily transformed into a simple geometric description, namely Ewald sphere, as shown in Fig. 2.18.

In the experiment, the XRD diffractometer has a complicated three-dimensional (3D) configuration with many tunable perimeters and different kinds of scanning modes. The use of Ewald sphere has largely simplified the 3D configuration and is helpful for understanding the relationship between different perimeters in XRD. The real space parameters in the 3D configuration of XRD include incident vector  $\mathbf{K}_0$ , diffraction vector  $\mathbf{K}$ , diffraction angle  $2\theta$ , and the orientation angle of the sample surface  $\omega$ , while in the reciprocal space, parameters are reduced to a simple reciprocal vector  $\mathbf{Q}$  with two orthonormal components, i.e.,  $Q_z$  and  $Q_x$ , as shown in Fig. 2.19.

According to the relationship between the real space coordinates and reciprocal space coordinates, transformation of the parameters in real space and reciprocal space can be deduced as follows:

$$\begin{aligned} Q_x &= K[\cos(\theta - \omega) - \cos(\theta + \omega)] \\ Q_z &= K[\sin(\theta - \omega) - \sin(\theta + \omega)] \end{aligned} \quad (2.1)$$

in which  $K = 2\pi/\lambda$  is the radius of the Ewald sphere and is also used as the primitive vector in reciprocal space. The restrictions in the reciprocal space, which are determined by Bragg's law and the geometrical configuration in real space, can be expressed as follows:

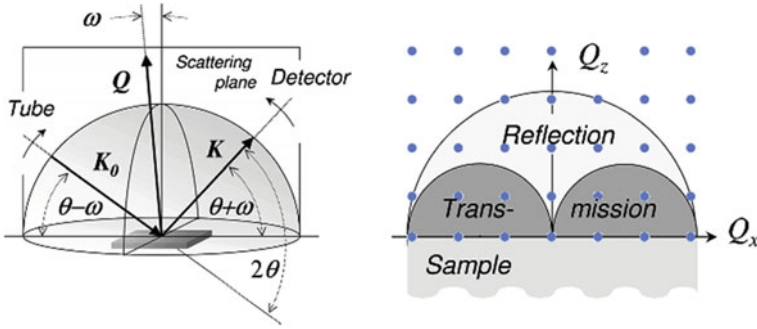


**Fig. 2.19** Parameter corresponding between real space (left) and reciprocal space (right) (Reproduced from Ref. [26] with permission from John Wiley & Sons Ltd.)

$$\begin{aligned}
 -2K &\leq Q_x \leq 2K \\
 0 &\leq Q_z \leq 2K \\
 Q_x^2 + Q_z^2 &\leq 4K^2
 \end{aligned} \tag{2.2}$$

The common scanning modes of XRD have three different cases, including  $\theta$ - $2\theta$  linkage scanning,  $\omega$  scanning (also known as the rocking curve scanning), and  $\omega$ - $2\theta$  linkage scanning (a kind of 2D mapping scanning, also known as the reciprocal space mapping, RSM [27]).

The  $\theta$ - $2\theta$  linkage scanning is the most commonly used scanning method in XRD, in which the direction of the incident X-ray is fixed and the Bragg diffraction condition is achieved by rotating the sample and the detector in the diffraction plane. When the sample rotates an angle  $\theta$ , the detector has to rotate  $2\theta$  in order to meet the Bragg condition. As a result, this kind of scanning mode is called  $\theta$ - $2\theta$  linkage. In the reciprocal space, this kind of scanning mode corresponds to an equivalent motion that the reciprocal diffraction vector  $Q$  scans in one dimension along the  $Q_z$ -axis, as shown in Fig. 2.20a. Thereby, the crystal information and lattice parameter perpendicular to the sample surface can be detected.

The  $\omega$  scanning or rocking curve scanning refers to a kind of scanning method in which the directions of the incident X-ray and X-ray detector are fixed at the position that a certain diffraction peak appears, and the Bragg diffraction condition is achieved by rocking the normal direction of the sample surface in the diffraction plane. In the reciprocal space, this kind of scanning mode corresponds to an equivalent motion that the reciprocal diffraction vector  $Q$  takes a one-dimensional scanning along the arc of a circle with the radius  $Q$ , as shown in Fig. 2.20b. According to the rocking curve obtained from the  $\omega$  scanning, full width at half maximum (FWHM) of the diffraction peak can be deduced, which is an important index to characterize the quality of a crystal sample. Generally speaking, if the FWHM value of a crystal sample is small, i.e., the corresponding rocking curve is narrow, the crystal is supposed to be in a good uniformity and crystallinity.

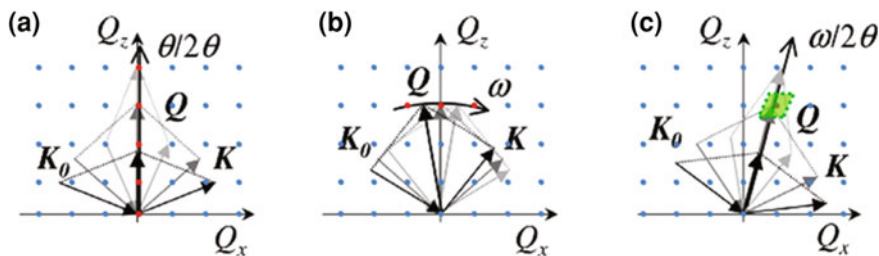


**Fig. 2.20** Reciprocal space configurations of the three kinds of scanning methods: **a**  $\theta$ - $2\theta$  linkage scanning, **b**  $\omega$  scanning, and **c**  $\omega$ - $2\theta$  linkage scanning (Reproduced from Ref. [26] by permission of John Wiley & Sons Ltd.)

The  $\omega$ - $2\theta$  linkage scanning (RSM scanning) is a kind of scanning method that combines the  $\theta$ - $2\theta$  linkage with the  $\omega$  scanning, and the detailed operation process is described as follows. First, the normal direction of the sample surface is fixed at a certain angle  $\omega$ , and then the  $\theta$ - $2\theta$  linkage scanning is performed. After that, the normal direction of the sample surface is rotated to another angle  $\omega + \Delta\omega$ , and then the  $\theta$ - $2\theta$  linkage scanning is performed for another time. Repeating the above process by continuously taking the  $\theta$ - $2\theta$  linkage scanning under stepping changed  $\omega$  value, the  $\omega$ - $2\theta$  linkage scanning can be achieved. In the reciprocal space, this kind of scanning mode corresponds to an equivalent motion that the reciprocal diffraction vector  $\mathbf{Q}$  takes a two-dimension scanning in a small parallelogram around a reciprocal lattice point, as shown in Fig. 2.20c. Utilizing this kind of scanning method, various information about the crystal sample such as the in-plane and out-of-plane lattice parameters, quality of the epitaxial film, and elastic distortion of the unit cell can be quantitatively or qualitatively determined from the RSM results, which have vital significance and wide applications in material science [28, 29].

In addition to the three kinds of scanning methods described above, there is another kind of scanning mode in XRD named  $\varphi$  scan, in which the sample has to rotate along its surface normal direction ( $\varphi$ ) to meet the Bragg diffraction condition. In  $\varphi$  scan, the directions of the incident X-ray and X-ray detector are fixed at the positions that meet the diffraction condition of a certain crystal face, and the selected crystal face is always not parallel to the sample surface but is at an angle to it. In the sample rotation along its surface normal direction, diffraction peaks can be detected whenever the selected crystal face or the equivalent one appears. As a result, the in-plane symmetry of the sample and the relative lattice orientation between the epitaxial film and the single crystal substrate can be detected by the  $\varphi$  scanning method.

The model of X-ray diffractometer employed in the investigations related to the thesis is Rigaku-D/max-RB, equipped with Cu target as the emitter of X-ray with the wavelength of  $K_\alpha \sim 1.5406 \text{ \AA}$ . To realize high-quality X-ray with good parallelism and single wavelength for accurate XRD measurement, restrictive slits

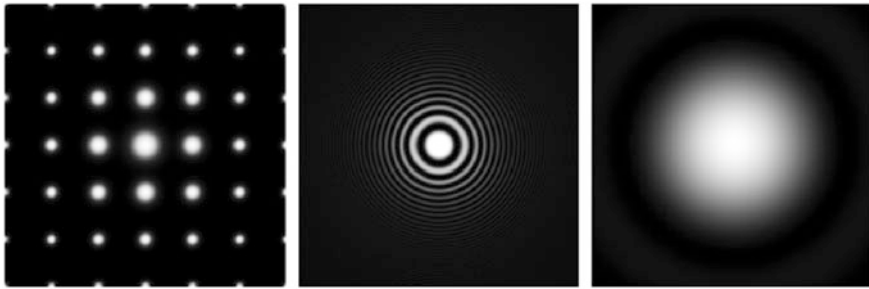


**Fig. 2.21** Three kinds of diffraction patterns in TEM (simulated results): single crystal (*left*), polycrystalline (*middle*), and amorphous (*right*)

and monochromators are placed in the emitter and detector of X-ray. In the measurement of polycrystalline samples, the size of slits are set as follows: emitting slit  $1^\circ$ , receiving slit  $1^\circ$ , and divergence slit 0.3 mm. As for the measurement of single crystals or epitaxial thin films, the value of each slit should be reduced by half and attenuation sheet should be inserted into the detector to protect the instrument due to the high diffraction intensity. What is more, other kinds of X-ray diffractometer have also been used by the collaborators in Hefei and Shanghai light source to accomplish part of this thesis work, which is not elaborated here.

In the characterization techniques for the micro-/nano-structures, there is another powerful instrument named *transmission electron microscope (TEM)*, which has ultra-high resolution and the ability of atomic level imaging. The basic principle of TEM is similar to the optical microscope, except the fact that electron beam is used as the light source and electric/magnetic fields are used as lens in the TEM imaging. Since the wavelength of the electrons is very small, image with atomic-scale resolution can be obtained by the TEM technique. However, as the penetrating ability of the electron beam is weak, samples to be characterized by TEM have to be prepared into ultra-thin slices (generally less than 100 nm), which is a difficult task. In addition to directly imaging the samples at the atomic level, TEM has another basic function of carrying out the electron diffraction. Similar to X-ray diffraction, the behavior of electron diffraction also obeys the Bragg's law  $2d \cdot \sin(\theta) = n\lambda$ , only the  $\lambda$  here is the wavelength of electrons. From the diffraction pattern of TEM, the crystal morphology and structure of the sample can be easily determined, which can be divided into three kinds of categories with different diffraction patterns, including single crystal, polycrystalline, and amorphous structure, as shown in Fig. 2.21. The diffraction pattern of the single crystal sample consists of ordered lattices, i.e., the reciprocal lattice of the single crystal. The diffraction pattern of the polycrystalline sample consists of many concentric rings, in which the finer the ring is, the larger the grain size will be. The diffraction pattern of the amorphous sample exhibits a diffuse halo-like form, due to the absence of ordered crystal lattice inside the materials.

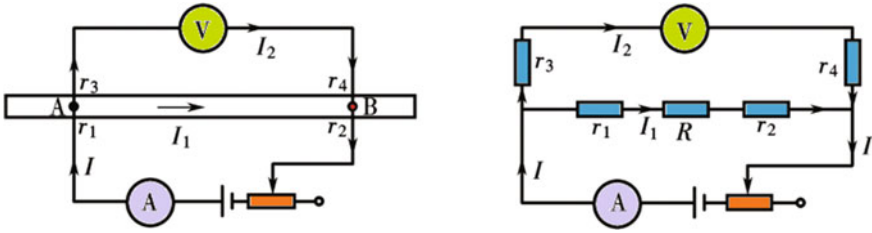


**Fig. 2.22** Two-wire method for the resistance measurement: schematic circuit (*left*) and equivalent circuit (*right*)

### 2.2.5 Electrical Transport Measurement Technique and Photolithography

The most frequent task in the electrical experiments is the measurement of resistance. There are a lot of factors that affect the accuracy of resistance measurement. For example, the precision of instrument is one of the key factors, and on the other hand, the design of measurement circuit is also important which is related to the contact resistance. Generally, the two-wire method is often adopted in resistance measurements, as shown in Fig. 2.22.

In the circuit,  $R$  is the true resistance of the sample,  $r_1$  and  $r_2$  are the contact resistance induced by the access of current,  $r_3$  and  $r_4$  are the contact resistance induced by the access of voltmeter. The internal resistance of an ideal voltmeter in circuit can be considered as infinity; therefore, the currents in the two-wire circuit satisfy the following relations:  $I_2 \ll I_1$  and  $I_1 - I$ . As for the voltage measurement, the visual value is equal to  $U_{r1} + U_R + U_{r2}$ , and therefore, the calculated resistance of the sample is  $r_1 + R + r_2$ . If the resistance of the sample is very large, i.e.,  $R \gg r_1$  and  $R \gg r_2$ , the result of the two-wire measurement is approximate to the true value  $R$ . However, in the case that  $R$  is small or high requirement of measurement precision, e.g., the measurement of magnetoresistance in CoFeB structures, the two-wire method is no longer viable. The contact and lead resistance in circuit cannot be avoided, but can be eliminated by a so-called four-wire method as shown in Fig. 2.23, which is important to measure the resistivity of metal or semiconductor materials.

In the case that all the conditions in the two-wire and four-wire circuits, such as the sample resistance  $R$ , the contact resistance  $r_1, r_2, r_3, r_4$ , and the equivalent condition  $I_1 - I$  for an ideal voltmeter, are similar to each other, one can see that the visual voltage is  $U_R$  and the calculated resistance is  $R$ , which is equal to the true value of the sample, as revealed from the equivalent circuit in Fig. 2.23b.

In this thesis, the involved measurements of magnetoresistance and investigation of the electric field control of magnetization in the CoFeB/PMN-PT structure are carried out in the MPMS, which provides a stable and controllable magnetic field and temperature environment. Different kinds of electrometers are integrated with MPMS and employed in the four-wire method, in which Keithley 2400 is

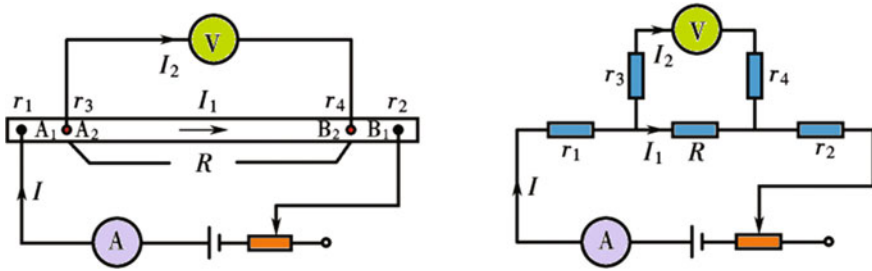


**Fig. 2.23** Four-wire method for the resistance measurement: schematic circuit (*left*) and equivalent circuit (*right*)

used as the constant current source, Keithley 2182 is used as the voltmeter, and Keithley 6517A is used for applying high voltage. Moreover, lithography technique and mask design are also needed for the preparation of spintronic devices. Since this part of work is done by collaborators, the lithography technique is not described here.

## References

1. D. Dijkkamp, T. Venkatesan, X.D. Wu et al., Preparation of Y-Ba-Cu-O oxide superconductor thin films using pulsed laser evaporation from high  $T_c$  bulk material. *Appl. Phys. Lett.* **51**, 619–621 (1987)
2. D.B. Chrisey, G.K. Hubler, *Pulsed Laser Deposition of Thin Films* (Wiley-Interscience, New York, 1994)
3. L.W. Martin, Y.H. Chu, R. Ramesh, Advances in the growth and characterization of magnetic, ferroelectric, and multiferroic oxide thin films. *Mater. Sci. Eng. R-Reports* **68**, 133 (2010)
4. M. Kanai, T. Kawai, S. Kawai, Atomic layer and unit cell layer growth of (Ca, Sr)CuO<sub>2</sub> thin film by laser molecular beam epitaxy. *Appl. Phys. Lett.* **58**, 771–773 (1991)
5. P.J. Kelly, R.D. Arnell, Magnetron sputtering: a review of recent developments and applications. *Vacuum* **56**, 159–172 (2000)
6. W.J. Xu, Recent developments and applications in magnetron sputtering. *Mod. Instrum.* **5**, 1–10 (2005). (in Chinese)
7. J. Clarke, SQUID: for superconducting quantum interference devices. *Sci. Am.* **271**, 46 (1994)
8. M. Mcelfresh, *Fundamentals of Magnetism and Magnetic Measurements* (Purdue University, Quantum Design, USA, 1994)
9. J.J. Yang, Tunability of the electric and magnetic properties in multiferroic heterostructures. Doctoral Thesis, Tsinghua University, 2010. (in Chinese)
10. W. Ning, Investigation of perovskite manganites by electron spin resonance. Doctoral Thesis, Institute of Physics CAS, 2008. (in Chinese)
11. J. Lee, J. Jeong, D. Kim et al., Three-configurational surface magneto-optical Kerr effect measurement system for an ultrahigh vacuum in situ study of ultrathin magnetic films. *Rev. Sci. Instrum.* **71**(10), 3801–3805 (2000)

12. G. Ornelas-Arciniega, J. Reyes-Gomez, A.G. Castellanos-Guzman, A new modification to the Sawyer-Tower ferroelectric hysteresis loop tracer. *J. Korean Phys. Soc.* **32S**, S380–S381 (1998)
13. S.M. Feng, Y.S. Chai, J.L. Zhu et al., Determination of the intrinsic ferroelectric polarization in orthorhombic  $\text{HoMnO}_3$ . *New J. Phys.* **12**, 073006 (2010)
14. M. Fukunaga, Y. Noda, New technique for measuring ferroelectric and antiferroelectric hysteresis loops. *J. Phys. Soc. Jpn.* **77**, 064706 (2008)
15. T. Wu, A. Bur, P. Zhao et al., Giant electric-field-induced reversible and permanent magnetization reorientation on magnetoelectric  $\text{Ni}/(011)[\text{Pb}(\text{Mg}_{1/3}\text{Nb}_{2/3})\text{O}_3](1-x)-[\text{PbTiO}_3]x$  heterostructure. *Appl. Phys. Lett.* **98**, 012504 (2011)
16. J. Ma, Y.H. Lin, C.W. Nan, Anomalous electric field-induced switching of local magnetization vector in a simple  $\text{FeBSiC-on-Pb(Zr, Ti)O}_3$  multiferroic bilayer. *J. Phys. D-Appl. Phys.* **43**, 012001 (2010)
17. C. Thiele, K. Dorr, O. Bilani et al., Influence of strain on the magnetization and magnetoelectric effect in  $\text{La}_{0.7}\text{A}_{0.3}\text{MnO}_3/\text{PMN-PT}(001)$  ( $\text{A} = \text{Sr, Ca}$ ). *Phys. Rev. B* **75**, 054408 (2007)
18. Z.Y. Feng, D. Lin, H.S. Luo et al., Effect of uniaxial stress on the electromechanical response of  $\langle 001 \rangle$ -oriented  $\text{Pb}(\text{Mg}_{1/3}\text{Nb}_{2/3})\text{O}_3\text{-PbTiO}_3$  crystals. *J. Appl. Phys.* **97**, 024103 (2005)
19. L. Han, H.M. Chen, X.F. Wang, The application of the scanning probe microscopy in the GaAs semiconductor. *Funct. Mater.* **2**, 32–35 (1999). (in Chinese)
20. V.L. Mironov, *Fundamentals of Scanning Probe Microscopy* (Institute of Physics of Microstructures, The Russian Academy of Science, Nizhniy Novgorod, 2004)
21. H. Zhong, Quantitative investigation of magnetic nanostructures by magnetic force microscopy. Doctoral Thesis, Tsinghua University, 2009. (in Chinese)
22. N. Balke, I. Bdikin, S.V. Kalinin et al., Electromechanical imaging and spectroscopy of ferroelectric and piezoelectric materials: state of the art and prospects for the future. *J. Am. Ceram. Soc.* **92**(8), 1629–1647 (2009)
23. J.Y. Dai, J.X. Wang, Study of the ferroelectric domain structure and evolution in PMN-30 % PT single crystal by means of piezoresponse force microscopy (in English). *Prog. Phys.* **2**, 197–214 (2009)
24. F. Zavaliche, S.Y. Yang, T. Zhao et al., Multiferroic  $\text{BiFeO}_3$  films: domain structure and polarization dynamics. *Phase Transitions* **79**, 991–1017 (2006)
25. S. Anders, H.A. Padmore, R.M. Duarte et al., Photoemission electron microscope for the study of magnetic materials. *Rev. Sci. Instrum.* **70**, 3973–3981 (1999)
26. M. Birkholz, P.F. Fewster, C. Genzel, *Thin Film Analysis by X-Ray Scattering* (WILEY-VCH Verlag GmbH, Weinheim, 2006)
27. P.F. Fewster, Reciprocal space mapping. *Crit. Rev. Solid State Mater. Sci.* **22**, 69–110 (1997)
28. H.J. Liu, P. Yang, K. Yao et al., Twinning rotation and ferroelectric behavior of epitaxial  $\text{BiFeO}_3$  (001) thin film. *Appl. Phys. Lett.* **96**, 012901 (2010)
29. G.Y. Gao, S.W. Jin, W.B. Wu, Lattice-mismatch-strain induced inhomogeneities in epitaxial  $\text{La}_{0.7}\text{Ca}_{0.3}\text{MnO}_3$  films. *Appl. Phys. Lett.* **90**, 012509 (2007)

Electric-Field Control of Magnetization and Electronic  
Transport in Ferromagnetic/Ferroelectric  
Heterostructures

Zhang, S.

2014, XVI, 130 p. 112 illus., 30 illus. in color., Hardcover

ISBN: 978-3-642-54838-3